

Core/shell nanostructures due to Ce into CoFe_2O_4 induce lattice and vibrational defects for magnetic and dielectric enhancement

Kuldeep Chand Verma^{1*}, R.K. Kotnala²

¹Centre of Advanced Study in Physics, Department of Physics, Panjab University, Chandigarh 160014, India

²CSIR-National Physical Laboratory, New Delhi 110012, India

*Corresponding author. Tel.: (+91) 9418941286; E-mail: kuldeep0309@yahoo.co.in, dkuldeep.physics@gmail.com

Received: 05 November 2015, Revised: 08 January 2016 and Accepted: 27 May 2016

ABSTRACT

We reported the Core/Shell structures of $\text{CoFe}_{2-x}\text{Ce}_x\text{O}_4$ (CFCeO) nanoparticles were prepared by a chemical combustion method. The Rietveld refinement of X-ray diffraction pattern results into CoFe_2O_4 spinel structure and the variation in lattice parameters have been found with doping of Ce ions. Transmission Electron Microscopy analysis has shown Core/Shell type nanoparticles. The stoichiometric composition of Co, Fe, Ce and O atoms has been analyzed through X-ray fluorescence elemental detection. Fourier transform infrared spectra could detect organic extent, tetrahedral (Fe-O), octahedral (Fe(Ce)-O-Co) and lattice disorder in CFO nanoparticles with Ce doping. Defects related oxygen vacancies are analyzed in Photoluminescence emission spectra. The room temperature magnetic measurement of CFO nanoparticles is highly influenced with Ce ions. The magnetic interactions are antiferromagnetic at room temperature that confirmed by zero field cooling and field cooling magnetic measurements at 100 Oe. However, the spin glass and ferromagnetic clustered growth may also exist in CFCeO samples that reduce room temperature ferromagnetism. The dielectric measurement indicates polarization up to higher frequency region that enhanced with Ce ions. Copyright © 2016 VBRI Press.

Keywords: Core/shell nanoparticles; magnetism; chemical combustion; rietveld refinement; defects.

Introduction

Recently, magnetic nanoparticles of CoFe_2O_4 (CFO) are extensively studied due to their potential utilization for high-density magnetic storage and spintronic devices [1-3]. CFO has an inverse spinel structure with cubic unit cell ($a = 8.391 \text{ \AA}$ at 300 K) of $Fd\bar{3}m$ space group [4]. At below the Curie temperature ($T_c \sim 860 \text{ K}$), CFO has long-range collinear ferrimagnetic order. Local canting and anisotropy reduces the moment to $3.35 \mu_B$ at 300 K, and the easy magnetization axis is along [100]. Guillot *et al.* [5] suggested six exchange parameters, between tetrahedral Fe^{3+} (A), octahedral Fe^{3+} (B') and Co^{2+} (B'') of spinel AB_2O_4 . This is proposed by molecular field model which led to anti ferromagnetic exchange constants $J \approx -20 \text{ K}$ (J_{AA} , J_{AB} , $J_{AB'}$, $J_{BB'}$, $J_{BB''}$) except for $J_{B''B''} \approx +40 \text{ K}$.

More recently, the formation of superparamagnetism with size reduction to the single phase CFO nanoparticles imposes a lower threshold in the grain size to maintain thermal stability of the magnetization [6]. Sun *et al.* [7] suggested spin-phonon coupling constant $\sim 6.3 \text{ N/m}$ for the bulk CFO and shown superparamagnetism between 7 and 10 nm. It means that superparamagnetism is enhanced ferromagnetic interactions either by varying size of CFO nanoparticles or ionic modifications [8]. Lima *et al.* [2] suggested that the interface formation in anti ferromagnetic (CoO)-core/ferrimagnetic (CFO)-shell nanoparticles have anisotropy enhanced with respect to the single phase counterparts. This core/shell interface has exchange coupling effects which increase the effective magnetic anisotropy in the system [9].

It is reported that the partial substitution of Fe^{3+} by rare earth (RE) ions in the spinel structure leads to structural distortion that induce strain to modify the dielectric behavior [10]. Lohar *et al.* [11] introduced RE-Fe ($4f-3d$) interactions in the spinel lattice which led to small change in the magnetization and T_c value. But the weak RE-RE ions interactions are observed. Zhang *et al.* [12] reported the lattice distortion and cation disorder in the spinel structure due to incorporation of Eu and Ce ions into Fe^{3+} and a huge ionic size difference between them cause large lattice defects. In RE ions, Ce has $4f$ electrons which are tightly bound around the nucleus and shielded by $5s^2 6d^1 6s^2$ electrons, leading to strong local spin. But it is difficult for Ce substituted CFO nanoparticles to perform $4f-4f$ and $4f-3d$ exchange interaction without a medium. Therefore, the defects/vacancies in the lattice become the medium of exchange interactions [13]. Recently, we have reported that the $\text{Ce}^{3+/4+}$ ionic formation via oxygen vacancy is anti ferromagnetic in nature [14].

In this paper, we have reported the synthesis, crystalline structure, micro structural, stoichiometric composition, vibrational, luminescent, magnetic and dielectric properties of $\text{CoFe}_{2-x}\text{Ce}_x\text{O}_4$ [$x = 0.05$ (CFCeO05), 0.1 (CFCeO10), 0.3 (CFCeO30) and 0.5 (CFCeO50)] nanoparticles.

Experimental

Sample preparation

The $\text{CoFe}_{2-x}\text{Ce}_x\text{O}_4$ nanoparticles were prepared by chemical combustion synthesis route using cobalt nitrate, ferric

nitrate, cerium chloride, polyethylene glycol (PEG) and urea taken in desired stoichiometric ratios to $\text{CFCeO}_{0.5}$, CFCeO_{10} , CFCeO_{30} and CFCeO_{50} . To prepare a precursor solution, cobalt nitrate, ferric nitrate and cerium chloride were added to PEG and it kept for stirring and raised the room temperature to 50°C . Urea was added to it and the temperature was then raised to 70°C till combustion take place. The nitrates were acting as oxidising agents and PEG and urea were reducing agents. Brown powder so obtained was purified by washing with a mixture of ethanol and water (double distilled) and finally subjected to annealing at 500°C for 5hrs.

Characterization techniques

The crystalline structure was analyzed by X-ray diffraction (XRD) (using X'Pert PRO PANalytical system) and microstructure by Transmission Electron Microscopy (TEM) (using HITACHI H-7500 system). Elemental analyses of the samples were performed through X-ray fluorescence (XRF) spectroscopy using Cu K_α radiation on WD-XRF (Model: S8 TIGER; Make: Bruker, Germany). The vibrational modes were detected by Fourier transform infrared (FTIR) spectrum on a Perkin Elmer system. Photoluminescence (PL) measurement was recorded on Renishaw system. Magnetization measurements were performed on Quantum Design SQUID-VSM system. For electrical measurements, the CFCeO crystalline powder was pressed into pellets of thickness ~ 0.5 mm by the cold isostatic pressing method with a pressure of 5 bar for 10 min and then sintered at 1000°C for 5 hrs. The dielectric measurement was performed on CFCeO pellet sample with frequency varying from 20 Hz to 120 MHz using Precision Impedance analyzer (Wayne Kerr 6500B).

Results and discussion

X-ray crystallography and Rietveld refinement

The Rietveld refinement of CFCeO nanoparticles were carried out in the spinel structure with cubic $Fd\bar{3}m$ space group. The Rietveld fit to the observed XRD pattern of CFCeO nanoparticles is depicted in **Fig. 1**. All the indices (h k l) in the XRD profile confirm single-phase spinel structure of CFO. The diffraction angle, $2\theta = 30.31, 35.63, 37.34, 43.27, 53.69$ and 57.21° corresponds to (220), (311), (222), (400), (422) and (511) planes (using JCPDS data), respectively, observed. The intensity of main diffraction peak of spinel CFO at (311) plane was considered as a measure of its degree of crystallinity. It is also assumed that the oxide phases CeO_2 and Ce_2O_3 may also appear in XRD patterns [core like formation in **Fig. 2**] which overlapped by highly intense peaks of the CFO phase. The CeO_2 has most intense XRD peaks (111) and (311) correspond to $2\theta = 28.57$ and 56.39° , respectively [15]. These peaks of CeO_2 may appear near (220) and (511) peaks of CFO phase in **Fig.1**. Also, the Bragg reflection (331) around 47.94° in the Rietveld analysis is not found in the experimental data. Most of the reported literature on CFO indicates that the (331) reflection has negligibly small or nil intensity in the XRD pattern [1-13]. The average crystallite size (D) of CFCeO samples was calculated by using Debye-Scherrer's formula ($D = \frac{0.94\lambda}{\beta \cos\theta}$); where λ , θ and β have their usual

meaning [16]. The size of nanoparticles, D, from (311) plane is 8, 12, 18 and 21 nm, and lattice constant (from Rietveld refinement) a (\AA) is 8.244 (1), 8.317 (3), 8.4044 (7) and 8.4403 (2), respectively, calculated for $\text{CFCeO}_{0.5}$, CFCeO_{10} , CFCeO_{30} and CFCeO_{50} sample. The values of lattice constants ($a=b=c$), unit cell volume (V), reliability factors (R_p , R_{wp} , R_{exp}), χ^2 , atomic position (x,y,z), bond length and bond angle of CFCeO samples are given in **Table 1**. All these structural parameters that refined from Rietveld fitting indicate variation as well as structural disorder of spinel structure of CFO with Ce doping. The increment in the nanoparticles size, D, and lattice constant, a , values with Ce doping in CFO is described due to larger ionic size of Ce^{3+} (1.01\AA) than Fe^{3+} (0.645\AA) and Co^{2+} (0.745\AA) ions.

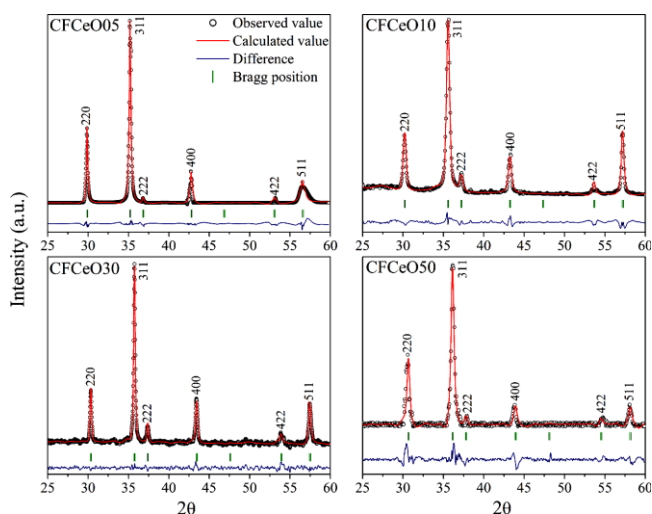


Fig. 1. Rietveld refinement of XRD data of $\text{CoFe}_{2-x}\text{Ce}_x\text{O}_4$ nanoparticles ($\text{CFCeO}_{0.5}$, CFCeO_{10} , CFCeO_{30} and CFCeO_{50}).

Table 1. Structural parameters obtained from Rietveld refinement of the XRD data of $\text{CoFe}_{2-x}\text{Ce}_x\text{O}_4$ nanoparticles for spinel structure with cubic $Fd\bar{3}m$ space group.

	CFCeO05	CFCeO10	CFCeO30	CFCeO50
$a = b = c$ (\AA)	8.244 (1)	8.317 (3)	8.4044 (7)	8.4403 (2)
V (\AA^3)	560.332 (2)	575.3077 (4)	593.6356 (8)	601.2757 (3)
R_p (%)	4.51	2.80	1.23	1.93
R_{wp} (%)	8.42	4.32	1.60	3.22
R_{exp} (%)	4.33	7.77	3.70	5.96
χ^2	3.78	0.309	0.187	0.292
atom Co				
$x/a = y/b = z/c$	0.1250	0.1250	0.1250	0.1250
atom Fe				
$x/a = y/b = z/c$	0.5000	0.5000	0.5000	0.5000
atom Ce				
$x/a = y/b = z/c$	0.5000	0.5000	0.5000	0.5000
atom O				
$x/a = y/b = z/c$	0.25108	0.2686	0.26286	0.24691
Bond length (\AA)				
Co-Fe	3.4179 (7)	3.4480 (10)	3.4843 (12)	3.49916 (7)
Co-Ce	3.4179 (7)	3.4480 (10)	3.4843 (12)	3.49916 (7)
Co-O	1.7408 (2)	1.9859 (4)	2.00681 (10)	1.84317 (3)
Fe-Fe	2.9148 (5)	2.9405 (8)	2.97140 (18)	2.98410 (5)
Fe-Ce	2.9148 (5)	2.9405 (8)	2.97140 (18)	2.98410 (5)
Fe-O	2.0868 (5)	3.4161 (7)	3.45201 (17)	2.10100 (5)
Ce-O	2.0868 (5)	3.4161 (7)	3.45201 (17)	2.10100 (5)
O-O	2.8427 (5)	3.2430 (8)	3.27710 (19)	3.00988 (5)
Bond angle (deg.)				
Fe-Co-Fe	50.479 (17)	50.48 (3)	50.479 (6)	50.4788 (17)
Fe-Co-O	79.98 (2)	79.98 (3)	79.975 (7)	79.975 (2)
Fe-Fe-Fe	60.000 (16)	60.00 (3)	60.000 (6)	60.000 (17)
Fe-Fe-O	134.30 (4)	138.017	138.011 (15)	135.248 (4)
Co-Fe-Co	62.964	62.96 (3)	62.964 (6)	62.964 (8)
Co-Fe-O	155.75 (5)	150.38 (8)	150.375 (19)	154.409 (5)
Co-Fe-Ce	64.761 (19)	64.76 (3)	64.761 (7)	64.7606 (20)
Co-Ce-Co	180.00 (5)	180.00 (7)	180.000 (17)	180.000 (5)
Ce-Ce-O	45.704 (19)	50.35 (3)	50.350 (6)	89.648 (2)
Ce-Ce-Ce	120.00 (3)	120.00 (11)	120.00 (11)	120.000 (3)

Nanostructural analysis and core/shell formation

Fig. 2 is the TEM images of CFCeO nanoparticles. It is shown that the distribution of nanoparticles in each sample is uniform. The average value of D is 8, 10, 19 and

20 nm, respectively, for CFCeO05, CFCeO10, CFCeO30 and CFCeO50 sample. The small size of the CFCeO nanoparticles is formed because we have used chemical combustion with low annealing of 500°C. It results into small growth of grains. Generally, nitrates serve as an excellent provider of oxidising environment. While the urea and PEG serve as reducing and chelating agents. PEG and urea gets chelation with metal ions. Formation of ammonium nitrate by the reaction of urea with metal nitrate ions helps in lowering of ignition temperature and provides combustion at low temperature with ease. PEG too gets chelated with metal ions and finally, the combustion takes place which led to nano-size product [17]. It has been also noticed that the core/shell type composite in TEM images (inset of Fig. 2 respectively) that shown random distributions of dark dots within a single nanoparticle. These dark dots may result from oxides of Ce ions (CeO_2) because their distribution has variation with increasing Ce doping. With higher Ce content into CFCeO50, a dispersion of Ce ions is found. A similar evolution of core/shell type formation has been given in the reported work [2].

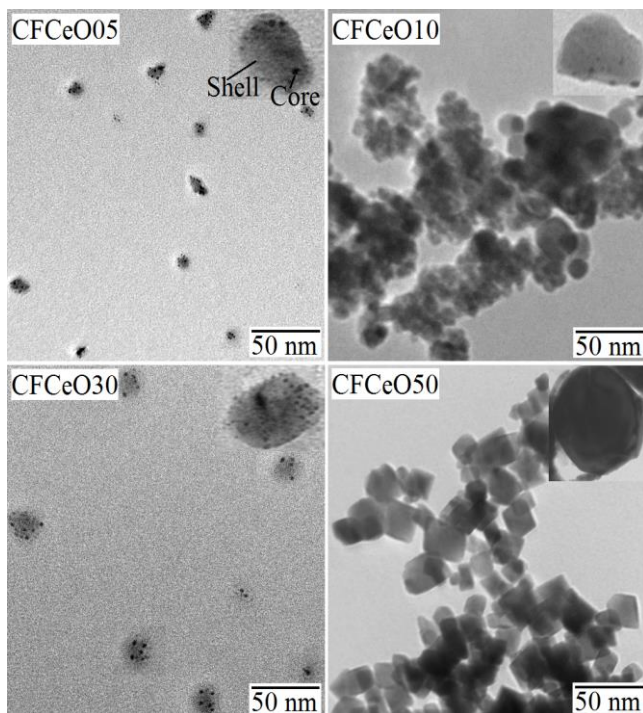


Fig. 2. TEM images of $\text{CoFe}_{2-x}\text{Ce}_x\text{O}_4$ ($x = 0.05, 0.1, 0.3$ and 0.5) nanoparticles. Inset shown Core-Shell formation, respectively.

Stoichiometric chemical composition of Co, Fe, Ce and O ions

A typical XRF pattern for Ce doped CFO nanoparticles is shown in Fig. 3. The pattern shows the presence of Co, Fe, Ce and O atoms of CFCeO with nominal concentration in each equal to the initial precursor composition. The composition of precursor solution is given in Table 2 which is assumed its theoretical values. The value of atomic concentration in weight percentage of each element is given in Fig. 3 (inset) that is compared with the theoretical composition (Table 2). The chemical

composition corresponding to Co, Fe and Ce ions show slight deviation with the theoretical one.

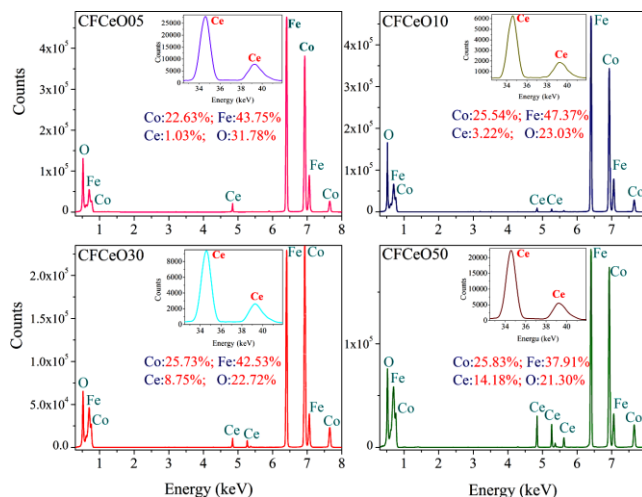


Fig. 3. Elemental analysis of Co, Fe, Ce and O of $\text{CoFe}_{2-x}\text{Ce}_x\text{O}_4$ ($x = 0.05, 0.1, 0.3$ and 0.5) nanoparticles using XRF pattern using Cu K_α radiation.

Table 2. Comparison of chemical composition (theoretical and experimentally observed values) of $\text{CoFe}_{2-x}\text{Ce}_x\text{O}_4$ ($x = 0.05, 0.1, 0.3$ and 0.5) nanoparticles calculated from elemental analysis given in Fig. 3 using XRF pattern of Cu K_α radiation.

Sample	chemical composition (theoretical value)	experimentally observed data (given in Fig.3) chemical composition*						
		Co	Fe	Ce	O	Co	Fe	Ce
CFCeO05	$\text{CoFe}_{1.99}\text{Ce}_{0.05}\text{O}_4$	22.63	43.75	1.03	31.78	1.01 ± 0.01	1.97 ± 0.05	0.046 ± 0.08
CFCeO10	$\text{CoFe}_{1.9}\text{Ce}_{0.1}\text{O}_4$	25.54	47.37	3.22	23.03	1.01 ± 0.01	1.88 ± 0.01	0.127 ± 0.27
CFCeO30	$\text{CoFe}_{1.7}\text{Ce}_{0.3}\text{O}_4$	25.73	42.53	8.75	22.72	1.02 ± 0.05	1.65 ± 0.02	0.342 ± 0.14
CFCeO50	$\text{CoFe}_{1.5}\text{Ce}_{0.5}\text{O}_4$	25.83	37.91	14.18	21.30	0.99 ± 0.01	1.46 ± 0.03	0.545 ± 0.09

*comparison with theoretical values and standard deviation

FTIR study

Fig. 4 shows the FTIR spectra of CFCeO nanoparticles at room temperature. A small intense peak at 3649 cm^{-1} is observed due to nonassociated O-H group. The broad absorption band at 3483 cm^{-1} is due to O-H...O stretching vibration. Weak absorption bands appear at 2852 and 2928 cm^{-1} are attributed due to symmetrical and asymmetrical stretching vibration of the aryl- CH_3 groups, respectively. The vibrational mode at 2359 cm^{-1} is assigned to CO_2 which is generally absorbed by magnetic nanoparticles from the environment. The highly intense absorption peak at 1596 cm^{-1} is corresponding to bending vibrations of the interlayer H_2O molecule. The weak vibrational modes in $1888\text{-}1729 \text{ cm}^{-1}$ are assigned to the carbonyl groups ($\text{C}=\text{O}$, $\text{C}=\text{C}$ etc). However, the vibrational modes in $1486\text{-}1229 \text{ cm}^{-1}$ region are attributed due to stretching vibrations of C-N, asymmetric and symmetric NO_2 and COO^- , CH_3 , CH_2 , NO_2^+ , NO_2^- etc [18]. These weak vibrational modes are formed during combustion process.

As shown in Fig. 4, the two new strong absorption bands between $650\text{-}450 \text{ cm}^{-1}$ are identified due to metal - oxygen spinel structure [18]. The higher 605 cm^{-1} is ν_1 due to intrinsic stretching at the tetrahedral site corresponds to Fe-O. The lower one at 467 cm^{-1} is ν_2 assigned to the octahedral-metal stretching [19] due to Fe(Ce)-O-Co. The observed trend in shifting ν_1 and ν_2 , and broadening of ν_2 reveal the incorporation of Ce ions into CFO lattice. It performs spectroscopic signatures of the transition of super

paramagnetism and surface spin disorder was observed by Sun *et al.* [7] for pure CFO. For ν_1 , the tetrahedral metal centers vibrate against the oxygen cage, and the octahedral metal centers vibrate against each other and the surrounding oxygen sites. For ν_2 , the tetrahedral metal center is fixed and oxygen cage vibration is balanced by octahedral cation + cage motion. Here, the octahedral metal center vibrates against the other B site cation and the surrounding oxygen centers. The splitting of tetrahedral ν_2 with varying Ce concentration might be strengthening spin-phonon coupling of CFO nanoparticles. This is due to core/shell formation of magnetic nanoparticles; spins align ferrimagnetically according to their exchange interactions [20], a process that mirrors the development of magnetic order in the bulk. Phonons that reside primarily in the core are sensitive to this magnetic structure, and they engage in spin-phonon coupling just like the bulk.

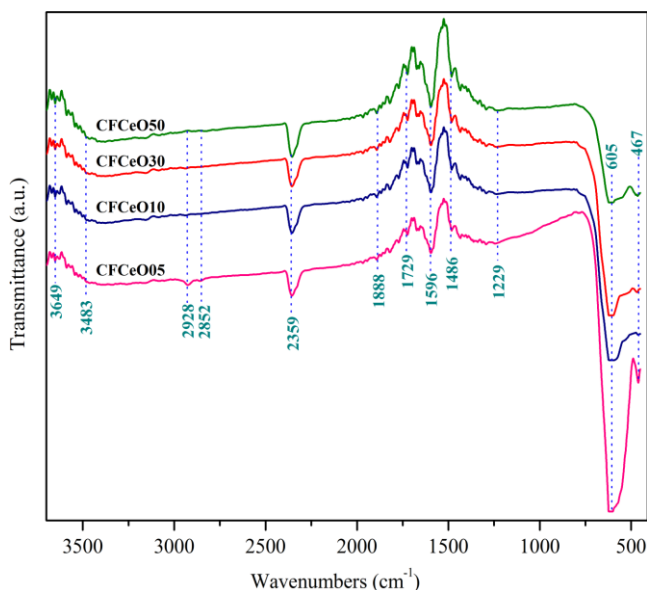


Fig. 4. FTIR spectra of $\text{CoFe}_{2-x}\text{Ce}_x\text{O}_4$ ($x = 0.05, 0.1, 0.3$ and 0.5) nanoparticles.

Energy band gap and defect carriers

Fig. 5 is the PL spectra of CFCeO nanoparticles measured at room temperature. In the UV wavelength region 200-400 nm, the emission peaks at 228, 246, 295 and 367 nm are observed. However, the peak at 216 nm is observed only in CFCeO50 due to the effect of lattice change and cation distribution. The peak at 367 nm is correlated with surface exciton recombination due to the characteristic of large specific surface area in the nanoparticles [21]. This peak of band gap energy is 3.38 eV which correspond to CeO_2 (3.40 eV). The emission intensity due to 216, 228, 246 and 295 nm are activated through photo-induced delocalization carriers which might be generates from nano grain boundaries, surfaces etc. It enhances localization of impurities and/or defect-trapped excitons.

In the visible region of **Fig. 5**, 400-700 nm, the highly intense emission peaks are violet [408 (3.04 eV) and 432 (2.87 eV) nm] and blue [458 nm (2.71 eV)] which correspond to band gap energy of pure CFO (2.7 eV) [22]. The violet luminescence occurs due to radiative defects related to interface traps existing at grain boundaries and

emitted from the radiative transition between interstitial metal (Co, Fe, Ce) levels and the valence band [23]. The blue emission exists due to electronic transition between interstitial metal ions vacancy. For more clarification, the inset of **Fig. 5** is also given corresponding to green (559 nm), yellow (583 nm), orange (601 nm) and red [625, 634, 648, 657, 675 and 692 nm] emission. It has been observed that the emission intensity broadens and sharpens, and shifting its position with Ce doping. This is related with surface defects of nanostructure, oxygen vacancy, metal ion vacancy etc. The green emission is originated from free-to-bound recombination between an electron from the conduction band edge with a hole from a trap level or the singly ionized oxygen vacancies at the particle surface. However, the yellow and orange emission is related to the doubly ionized oxygen vacancy. The red emission originates from the intrinsic defects of oxygen interstitials, which act as traps for photo-generated holes.

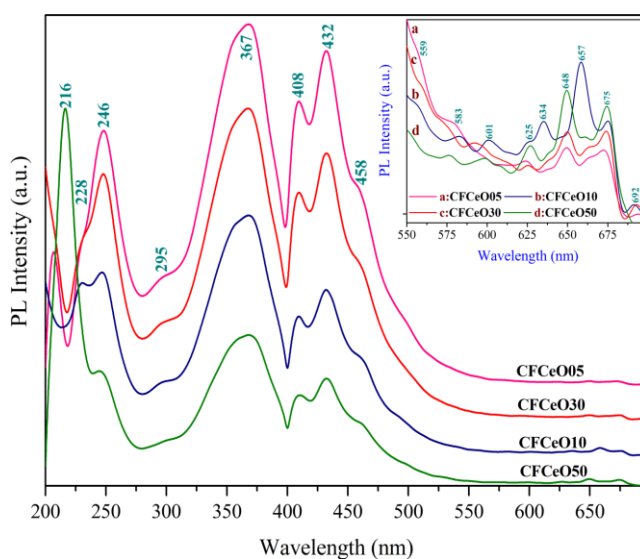


Fig. 5. PL spectra in wavelength region 200-700 nm and 550-700 nm [inset].

Magnetism

Fig. 6 (a-d) shows the magnetization-field (M - H) hysteresis of CFCeO nanoparticles measured at room temperature. The value of saturation magnetization, M_s , is 42.54, 10.41, 35.56 and 7.21 emu/g and remanent magnetization, M_r , is 26.68, 1.57, 19.07 and 0.25 emu/g, with coercivity, H_c , is 1526, 140, 1116 and 66 Oe, respectively, measured for CFCeO05, CFCeO10, CFCeO30 and CFCeO50 nanoparticles. These values of magnetization are enhanced than doped CFO nanoparticles [12, 24, 25] but smaller than bulk value that reported for pure CFO (73 emu/g at room temperature) [26]. This is due to higher surface energy and surface tension in the nanoparticles which result into change in cationic preferences of ferrite [27]. It leads to an increase in degree of anti-site defects which cause more surface spin canted or disorder and consequently, a significant reduction in the magnetization is obtained.

Recently, Georgiadou *et al.* [28] suggested modification in cation occupancy in nanostructural formation of spinel CFO. Due to this, the present samples must be involved

formula $[\text{Co}_{1-i}\text{Fe}_i]_A[\text{Ce}_{1-x}\text{Fe}_x]_{2-i}\text{BO}_4$, where i is the inversion degree and x is the concentration of Ce.

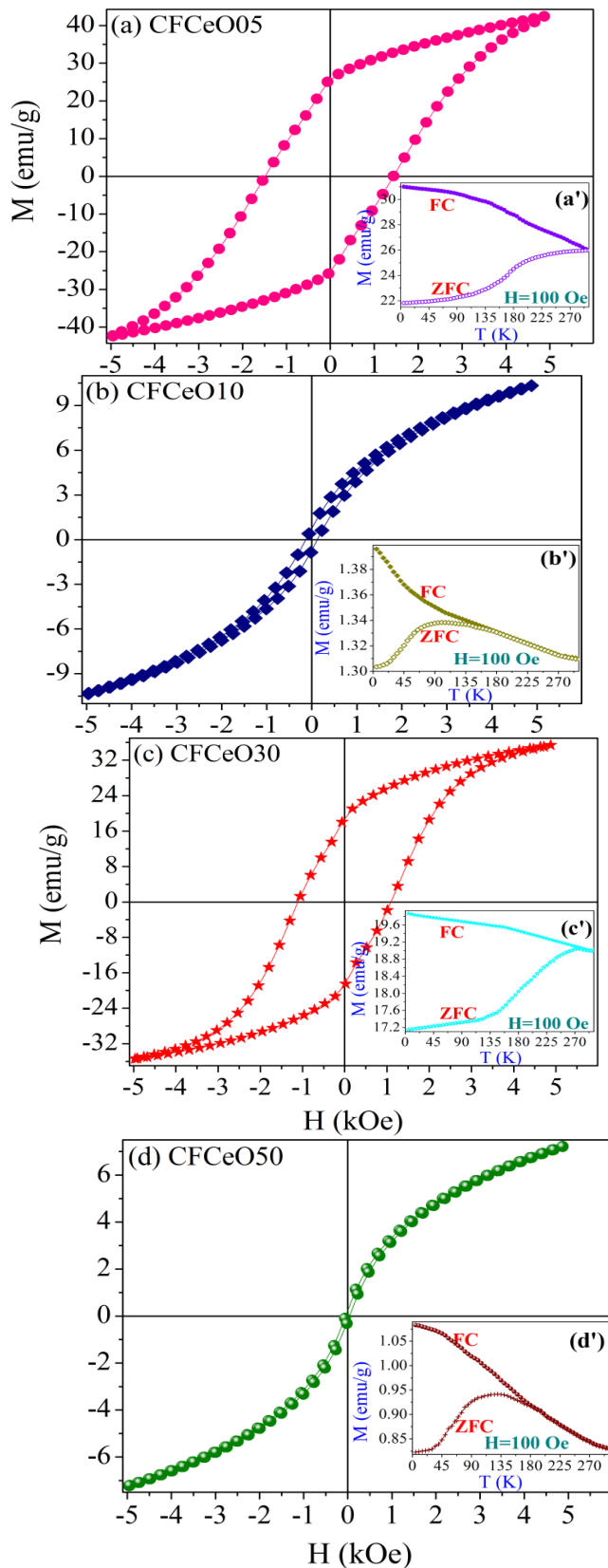


Fig. 6. M - H hysteresis measured at room temperature. Inset shows SQUID measurement for Zero-field cooled (ZFC)-field cooled (FC) experiment, performed at 100 Oe, showing the blocking temperature of spin glass and antiferromagnetic behaviors.

The theoretical expression for the net moment of M_{Ce} is given (Ce^{3+} ions occupy only the B sites for their large ionic size):

$$M_{\text{ce}} = M_{\text{B}} - M_{\text{A}} = [5 \times (1 - x) + 3.8 + x \times \mu_{\text{ce}}] - 5 \quad (1)$$

where M_{A} and M_{B} represent the total magnetic moment of the A and B sublattices, respectively. The magnetic moment of Fe^{3+} cation is fixed to $5\mu_{\text{B}}$ (spin only) and that of octahedrally coordinated Co^{2+} cations is fixed to 3.8 which correspond to the M_{s} at 0K of bulk CFO (95 emu/g) [29]. The net magnetic moments μ_{Ce} cation is zero for the diamagnetic Ce^{4+} ions and non-zero for the paramagnetic Ce^{3+} ones. By replacing Fe^{3+} by Ce^{3+} cation, the M_{s} is expected to vary as μ_{Ce} by the sequential filling of electrons in the 4f shell. Unlikely, a clear deviation between the theoretically predicted magnetization by equation (1) and the experimental one (**Fig. 6**) is observed. This is ascribed into two reasons. One is the decrease of the strong negative Fe^{3+} - Fe^{3+} interaction that resulted from the doping of Ce because the spinel ferrimagnetic CFO is largely governed by the negative Fe^{3+} - Fe^{3+} interaction (the spin coupling of the 3d electrons). The Ce^{3+} - Fe^{3+} interaction (4f-3d coupling) as well as the Ce^{3+} - Ce^{3+} one (indirect 4f-5d-4f coupling) exist but they are very weak [30]. The other is the rearrangement of the Co^{2+} ion in the A and B sites resulted from the doping with RECe^{3+} ions. The migration of Co^{2+} ion into tetrahedral sublattice decreases the concentration of Fe^{3+} ion in A site, leading to enhance M_{s} (**Fig. 6**) than calculated from equation (1).

As shown in **Fig. 6 (a-d)**, the value of H_{c} is reduces with Ce^{3+} ion concentration in CFCeO10 and CFCeO50 and shown weak ferromagnetism. This is responsible due to variation in core/shell formation (**Fig. 2**) and description of CFO lattice by vibrational modes (**Fig. 4**). Because the core/shell (CeO/CFO) system result into an increase in effective magnetic anisotropy caused by surface and interface exchange coupling effects [2]. The huge difference in the coercivity value among CFCeO samples may ascribe to surface pinning that arises due to missing coordination of oxygen atoms and the shape effect of the spinel ferrite. The cubic CFO nanoparticles are hypothesized to fewer missing oxygen atoms and less surface pinning, resulting into lower coercivity for the cubic structures [31]. The low value of M_{r} of CFCeO10 and CFCeO50 indicates the weak ferromagnetic behavior of the nanoparticles, which relax back their spins by rotation on removal of H so as to give a very low or nearly zero magnetic moment [32]. At the same time, the non-saturated magnetization suggests that the existence of strong antiferromagnetic inter-cluster interactions mixed with ferromagnetic interactions inside clusters [33]. This type of observed magnetism involves a similar behavior that was given by Pachpinde *et al.* [34] for their system of Pr^{3+} doped CFO. The magnetism of CFO must be related with Fe^{3+} -O- Fe^{3+} super exchange interaction strength and super-transfer fields, spin canting (non-collinear magnetic order), and magnetic dilution with valence state change of Fe^{3+} ($3d^5$ high spin) ions into Fe^{2+} ($3d^6$ low spin) ions by doping of Ce^{3+} ions. It is possible to involve Ce^{3+} - Fe^{3+} interactions via oxygen vacancies in 4f-3d coupling interactions which cause change in magnetism. The

replacement of Fe^{3+} ions by Ce^{3+} in the spin-up states may cause reduction in magnetization while spin-down states led to enhance magnetization [34]. The doping of Ce^{3+} - Fe^{3+} via oxygen also induces a perturbation in both electron-density and symmetry around the $2d$ lattice site. It could also be a possible to strengthen the exchange interactions and consequently enhance magnetization [33]. In these discussions, the origin of magnetism that shown in **Fig. 6** is controversial and further investigation is needed.

The origin of observed room temperature ferromagnetism of CFCEO samples is evaluated by the temperature dependent magnetization $[M(T)]$ with field cooling (FC) and zero field cooling (ZFC) measurement (**Fig. 6** (a'-d') inset). The applied magnetic field is 100 Oe. These M-T measurements show that ZFC-FC curves of the CFCEO05 and CFCEO30 sample did not coincide with each other or slightly coincide around 300 K. It indicates that the nanoparticles are still magnetically blocked at around room temperature. However, CFCEO10 and CFCEO50 nanoparticles show blocking temperature of antiferromagnetism, spin glass etc. at about 91 and 113 K, respectively. This type of the magnetic response is due to different nano-core/shell formation in CFCEO samples (**Fig. 2**). The Core/Shell nanoparticles provides spin-phonon coupling in which a Core of aligned spins is surrounded by a magnetically disordered shell [7]. The observed blocking temperature here may relate with Neel temperature, T_N of antiferromagnetic interaction and spin glass transition like behaviors. The antiferromagnetic interactions are formed due to Ce ions with oxygen vacancies and $4f$ - $3d$ transition between Ce and ferrimagnetic CFO [35]. The origin of the T_N is debated, and it is attributed by change in the dimensionality, surface and interface exchange coupling effects [36]. This enhance the surface exchange interaction because surface disorder in ferrite nanoparticles [37]. The higher T_N values are ascribed due to increase of the super exchange interaction and the cation disorder which increases the super exchange bond angle [38].

Moreover, the decrement in magnetization parameters in CFCEO10 and CFCEO50 is also ascribed due to their magnetic interactions that measured at low temperature by FC and ZFC (**Fig. 6** (b') and (d')). The lowering of temperature leads to the formation of a cusp in ZFC plot in both of the samples indicated by blocking or Neel temperature. A cusp in the ZFC plot and the distinctive separation of FC and ZFC data are typical features of spin glasses [39]. This is usually explained in terms of spin freezing or change in the spin-ordering leading to a spin-glass like phase formation at low temperatures. However, the splitting of the FC and ZFC curves is not a sufficient evidence to conclude spin-glass nature as it is also often observed in the ferromagnetic regions in many systems, attributed to the pinning of the domain walls. In both cases of superparamagnetic and spin glass, finite dipolar interaction between the spins results in the deviation of FC-ZFC curves at temperature lower than blocking or freezing temperatures and FC magnetization that increased continuously as the temperature is lowered [40]. The primary exchange mechanism in ferrite compounds is an antiferromagnetic super-exchange interaction between metal cations mediated by an intervening oxygen ion.

Because of the indirect nature of the coupling, the super-exchange interaction is sensitive to modified bond lengths and angles at a surface, and variation in coordination of surface cations will produce a distribution of net exchange fields [41]. We have recently reported that the oxygen vacancies or defects in a disordered state and a stronger competition between ferromagnetic and antiferromagnetic phases lead to a highly frustrated system, due to the melting of frozen magnetic moments in a random direction [42]. This can lead to a spin glass and ferromagnetic clustered behavior that is responsible for the cusp observed in the ZFC curve. Thus, the spin glass like behavior may responsible into observed weak ferromagnetism in CFCEO10 and CFCEO50 samples.

Furthermore, the existence of Ce^{3+} states may be the origin of variation in room temperature ferromagnetism in our work. In general, cerium is incorporated as paramagnetic Ce^{3+} and diamagnetic Ce^{4+} ions [43]. It is well-known that in the valence transfer change of cerium from +4 to +3 an unpaired spin in the Ce f orbitals is generated, and thus magnetism is induced. The exchange interaction between $4f$ unpaired electrons in Ce^{3+} and oxygen can result in antiferromagnetic interactions. It is also emphasized that an increase of Ce dopant produces higher disorder in Fe and Co structure due to increased oxygen vacancy and metal interstitials. It performs the existence of Ce^{3+} via oxygen vacancies with CFO ions which contribute antiferromagnetism or weak ferromagnetism at room temperature [44, 45]. The Ce^{3+} ion bears one localized $4f$ ($[xe] 4f^1$) electron, and its ordered magnetic moment is $2.16\mu_B$. As the particles size is reduced, the surface effects are prominent, and then the hybridization between Ce ions and Fe or Co ions is higher as expected in nanoparticles. Hence, the overlap of the Ce $4f$ and Fe $3d$ or Co $3d$ could enhance the paramagnetic or antiferromagnetic order at room temperature in Ce doped CFO samples.

Room temperature dielectric properties

Fig. 7 show the variation of dielectric constant (ϵ_r) and loss ($\tan\delta$) [inset] of CFCEO nanoparticles at room temperature. The large dispersion in ϵ_r at lower frequency is observed which is reducible with varying Ce doping. It is due to the predominance of interfacial dislocations, oxygen vacancies, grain boundary defects etc. While the decrease in ϵ_r with frequency follows the Maxwell-Wagner type interfacial polarization [46]. The value of ϵ_r at 10 MHz is 16, 18, 28 and 41, and $\tan\delta$ is 0.065, 0.103, 0.091 and 0.281, respectively, measured for CFCEO05, CFCEO10, CFCEO30 and CFCEO50. The increment in the value of ϵ_r is explained on the basis of varying particles size. The CFCEO05 and CFCEO30 show abrupt increment in both ϵ_r and $\tan\delta$ after 20 MHz is due to resonance effect [47]. While CFCEO10 and CFCEO50 have no such type of behavior up to 120 MHz. It is explained on the basis of different nanostructural formation [**Fig. 2**] and lattice disorder. The substitution of Ce^{3+} for Fe^{3+} produces hindrance to the polarization process and localizes the divalent ion in the lattice. This can affect the conduction mechanism and polarization which results into increasing conductivity and activation energy. Thus, variation in ϵ_r is observed and reported [48].

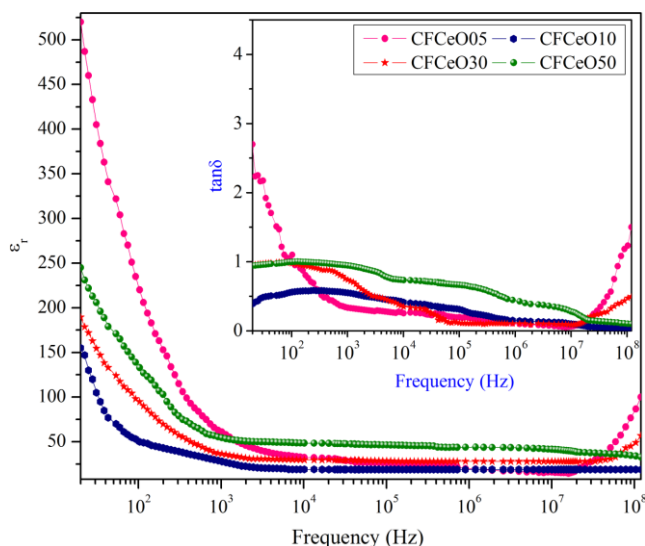


Fig. 7. Frequency dependent relative permittivity (ϵ_r) and loss ($\tan\delta$) of $\text{CoFe}_{2-x}\text{Ce}_x\text{O}_4$ ($x = 0.05, 0.1, 0.3$ and 0.5) nanoparticles.

Conclusion

The Core/Shell nanocomposites formation for CFCeO ferrite hinders the super paramagnetism formed due to small magnetic nanoparticles. The incorporation of Ce into CFO results into long-range antiferromagnetic interactions. XRD pattern shows spinel structure with cubic $Fd\bar{3}m$ space group of CFCeO. From TEM images, the average particles size, $D = 8, 10, 19$ and 20 nm, respectively, for CFCeO05, CFCeO10, CFCeO30 and CFCeO50 sample. XRF pattern measured the compositional stoichiometric ratio which is consistent with theoretical one that was taken in precursor solution of each sample. FTIR spectra show vibrational modes corresponding to tetrahedral and octahedral-metal stretching at 605 and 467 cm^{-1} , respectively. FTIR also observed some carbon related ions and O-H compounds and their extent must remove during heating in the form of H_2O or CO_2 . It results into defects formation on grain surfaces. The Ce ions take place disorder in spinel lattice also results into defects formations which are confirmed by PL emission. The defect acts as a medium of magnetic interactions. The CFCeO nanoparticles are suitable for storage devices at higher frequency and confirmed by dielectric measurement.

Acknowledgements

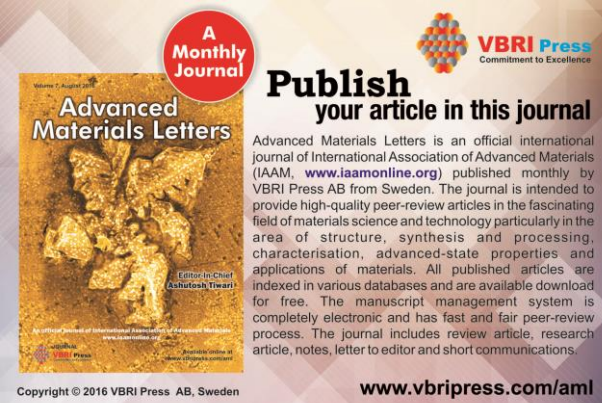
Kuldeep Chand Verma acknowledges SAIF/CIL Lab, Panjab University, Chandigarh, India, for providing XRD, TEM, FTIR facilities and Mr. Tejbir Singh for expert technical assistance of WD-XRF for the same.

Reference

- Tahar, L.B.; Artus, M.; Ammar, S.; Smiri, L.S.; Herbst, F.; Vaulay, M.J.; Richard, V.; Greneche, J.M.; Villain, F.; Fievet, F. *J. Magn. Magn. Mater.* **2008**, *320*, 3242.
- Lima, E.; Winkler, E.L.; Tobia, D.; Troiani, H.E.; Zysler, R.D.; Agostinelli, E.; Fiorani, D. *Chem. Mater.* **2012**, *24*, 512.
- Verma, K.C.; Singh, V.P.; Ram, M.; Shah, J.; Kotnala, R.K. *J. Magn. Magn. Mater.* **2011**, *323*, 3271.
- Teillet, J.; Bouree, F.; Krishnan, R. *J. Magn. Magn. Mater.* **1993**, *123*, 93.
- Guillot, M.; Ostorero, J.; Marchand, A. *Z. Phys. B Condensed Mat.* **1988**, *71*, 193.
- O'Handley, R.C. *Modern Magnetic Materials*; Wiley and Son: New York, **2000**.

- Sun, Q.C.; Birkel, C.S.; Cao, J.; Tremel, W.; Musfeldt, J.L. *ACS Nano* **2012**, *6*, 4876.
- Skumryev, V.; Stoyanov, S.; Zhang, Y.; Hadjipanayis, G.; Givord, D.; Nogues, J. *Nature (London)*. **2003**, *423*, 850.
- Berkowitz, A.E.; Takano, K. *J. Magn. Magn. Mater.* **1999**, *200*, 552.
- Gu, Z.; Xiang, X.; Fan, G.; Li, F. *J. Phys. Chem. C*. **2008**, *112*, 18459.
- Lohar, K.S.; Pachpinde, A.M.; Langade, M.M.; Kadam, R.H.; Shirsath, S.E. *J. Alloys Comp.* **2014**, *604*, 204.
- Zhang, Y.; Ma, J.; Lun, J.; Wen, D. *Cer. Int.* **2014**, *40*, 4437.
- Yao, B.; Wang, P.; Wang, S.; Zhang, M. *Cryst Eng Comm* **2014**, *16*, 2584.
- Verma, K.C.; Kotnala, R.K. *Phys. Chem. Chem. Phys.* **2016**, *18*, 5647.
- Enriquez, J.M.H.; Rodrigo, R.S.; Alamilla, R.G.; Serrano, L.A.G.; Handy, B.E.; Galindo, G.C.; Hernandez, A.C. *J. Mex. Chem. Soc.* **2012**, *56*, 115.
- Cullity, B.D. *Elements of X-Ray Diffraction* (Addison-Wesley, London), **1959**.
- Verma, K.C.; Singh, S.; Tripathi, S.K.; Kotnala, R.K. *J. Appl. Phys.* **2014**, *116*, 124103.
- Slatineanu, T.; Iordan, A.R.; Palamaru, M.N.; Caltun, O.F.; Gafton, V.; Leontie, L. *Mater. Res. Bull.* **2011**, *46*, 1455.
- Samoila, P.; Slatineanu, T.; Postolache, P.; Iordan, A.R.; Palamaru, M.N. *Mater. Chem. Phys.* **2012**, *136*, 241.
- Kodama, R.H.; Berkowitz, A.E.; McNiff, E.J.; Foner, S. *Phys. Rev. Lett.* **1996**, *77*, 394.
- Panigrahy, B.; Aslam, M.; Bahadur, D. *Nanotechnology* **2012**, *23*, 115601.
- Holinsworth, B.S.; Mazumdar, D.; Sims, H.; Sun, Q.C.; Yurtisigi, M.K.; Sarker, S.K.; Gupta, A.; Butler, W.H.; Musfeldt, J.L. *Appl. Phys. Lett.* **2013**, *103*, 082406.
- Jin, B.J.; Im, S.; Lee, S.Y. *Thin Solid Films*. **2000**, *366*, 107.
- Zhang, D.; Pu, X.; Gao, Y.; Su, C.; Li, H.; Li, H.; Hang, W. *Mater. Lett.* **2013**, *113*, 179.
- Boobalan, T.; Suriyanarayanan, N.; Pavithradevi, S. *Mater. Sci. Semi. Proc.* **2013**, *16*, 1695.
- Qu, Y.; Yang, H.; Yang, N.; Fan, Y.; Zhu, H.; Zou, G. *Mater. Lett.* **2006**, *60*, 3548.
- Rajendran, M.; Pullar, R.C.; Bhattacharya, A.K.; Das, D.; Chintalapudi, S.N.; Majumdar, C.K. *J. Magn. Magn. Mater.* **2001**, *232*, 71.
- Georgiadou, V.; Tangoulis, V.; Arvanitidis, I.; Kalogirou, O.; Samara, C.D. *J. Phys. Chem. C*. **2015**, *119*, 8336.
- Smith, S.; Wijn, H.P.J. *Ferrites*, Philips Library, Amsterdam, **1961**.
- Rezlescu, N.; Rezlescu, E.; Pansnicu, C.; Craus, M.L. *J. Phys.: Condens. Matter.* **1994**, *6*, 5707.
- Kolhatkar, A.G.; Jamison, A.C.; Litvinov, D.; Willson, R.C.; Lee, T.R. *Int. J. Mol. Sci.* **2013**, *14*, 15977.
- Gozuak, F.; Koseoglu, Y. *J. Magn. Magn. Mater.* **2009**, *321*, 2170.
- Ounnukad, S. *Solid State Commun.* **2006**, *138*, 472.
- Pachpinde, M.; Langade, M.M.; Lohar, K.S.; Patange, S.M.; Shirsath, S.E. *Chem. Phys.* **2014**, *429*, 20.
- Tang, Z.X.; Sorensen, C.M.; Klabunde, K.J.; Hadjipanayis, C.G. *Phys. Rev. Lett.* **1991**, *67*, 3602.
- Golosovsky, I.V.; Mirebeau, I.; Sakhnenko, V.P.; Kurdyukov, D.A.; Kumzerov, Y.A. *Phys. Rev. B*. **2005**, *72*, 144409.
- Yang, A.; Chinnasamy, C.N.; Greneche, J.M.; Chen, Y.J.; Yoon, S.D.; Chen, Z.H.; Hsu, K.L.; Cai, Z.H.; Ziemer, K.; Vittoria, C.; Harris, V.G. *Nanotechnology*. **2009**, *20*, 185704.
- Ponpandian, N.; Narayanasamy, A.; Chinnasamy, C.N.; Sivakumar, N.; Greneche, J.M.; Chattopadhyay, K.; Shinoda, K.; Jeyadevan, B.; Tohji, K. *Appl. Phys. Lett.* **2005**, *86*, 192510.
- Mukherjee, S.; Garg, A.; Gupta, R. *Appl. Phys. Lett.* **2012**, *100*, 112904.
- Xu, Q.; Sheng, Y.; Khalid, M.; Cao, Y.; Wang, Y.; Qiu, X.; Zhang, W.; He, M.; Wang, S.; Zhou, S.; Li, Q.; Wu, D.; Zhai, Y.; Liu, W.; Wang, P.; Xu, Y.B.; Du, J. *Sci. Rep.* **2015**, *5*, 1.
- Khurshid, H.; Lampen-Kelley, P.; Iglesias, O.; Alonso, J.; Phan, M.H.; Sun, C.J.; Saboungi, M.L.; Srikanth, H. *Sci. Rep.* **2015**, *5*, 1.
- Verma, K.C.; Kotnala, R.K. *Curr. Appl. Phys.* **2016**, *16*, 175.
- Okamura, Y.; Kubota, J.; Yamamoto, S. *IEEE Trans. Magn.* **1995**, *31*, 3289.
- Venkatesan, M.; Fitzgerald, C.B.; Coey, J.M.D. *Nature*. **2004**, *430*, 629.

45. Radovic, M.; Mitrovic, Z.D.; Paunovic, N.; Scepanovic, M.; Matovic, B.; Popovi, Z.V. *Acta Phys. Pol. A.* **2009**, *116*, 84.
46. Wagner, K.W. *Annals of Physics.* **2013**, *40*, 817.
47. Singh, S.; Singh, M.; Kotnala, R.K.; Verma, K.C. *Ind. J. Pure Appl. Phys.* **2014**, *52*, 550.
48. Nikumbh, A.K.; Pawar, R.A.; Nighot, D.V.; Gugale, G.S.; Sangale, M.D.; Khanvilkar, M.B.; Nagawade, A.V. *J. Magn. Magn. Mater.* **2014**, *355*, 201.



A Monthly Journal

Publish your article in this journal

Advanced Materials Letters is an official international journal of International Association of Advanced Materials (IAAM, www.iaamonline.org) published monthly by VBRI Press AB from Sweden. The journal is intended to provide high-quality peer-review articles in the fascinating field of materials science and technology particularly in the area of structure, synthesis and processing, characterisation, advanced-state properties and applications of materials. All published articles are indexed in various databases and are available download for free. The manuscript management system is completely electronic and has fast and fair peer-review process. The journal includes review article, research article, notes, letter to editor and short communications.

www.vbripress.com/aml

Copyright © 2016 VBRI Press AB, Sweden